ADVANCED MATERIALS
www.advmat.de

Vertical-Graphene-Reinforced Titanium Alloy Bipolar Plates in Fuel Cells

Feng Yu, Kun Wang, Lingzhi Cui, Shengli Wang, Ming Hou, Feng Xiong, Ruqiang Zou, Peng Gao, Hailin Peng, and Zhongfan Liu**

The bipolar plate (BP) serves as one of the crucial components in proton exchange membrane fuel cells (PEMFCs). Among BP materials, metallic BPs are widely employed due to their outstanding comprehensive properties. However, the interfacial contact resistance (ICR) between BP and gas diffusion layer together with corrosion of metallic BP under acidic operating conditions degrades the performance and stability of PEMFCs. Herein, an approach is proposed for the surface reinforcement of titanium (Ti) alloy BPs, relying on a directly grown vertical graphene (VG) coating via the plasma-enhanced chemical vapor deposition method. Compared with bare Ti alloy, the corrosion rate of VG-coated Ti alloy reduces by 1–2 orders of magnitude in the simulated PEMFC operating environments and ICR decreases by ≈100 times, while its thermal conductivity improves by ≈20% and water contact angle increases by 68.1°. The results can be interpreted that the unique structure of VG enables excellent electrical and thermal conduction in PEMFCs, and the highly hydrophobic VG coating suppresses the penetration of corrosive liquid as well as contributing to water management. This study opens a new opportunity to reinforce metallic surfaces by the robust and versatile VG coating for high-performance electrodes used in energy and catalyst applications.

1. Introduction

Proton exchange membrane fuel cells (PEMFCs) have emerged as the considerably promising energy conversion devices due to their high efficiency, zero pollution, and quick refueling.[1] As one of the crucial components in PEMFCs, the bipolar plate (BP) plays a significant role in supporting membrane electrode assembly, collecting current, transporting gas reactants, and enabling thermal and water management.[2] In terms of these functions, a good BP material is required to possess the characteristics of reliable mechanical strength, high electrical and thermal conductivities, low gas permeability, good hydrophobicity, etc. Traditional graphite BPs are hindered from the mass production and long-term use by their brittleness and large gas permeability.[3,4] In contrast, metallic BPs, such as stainless steel, aluminum, titanium (Ti), and their alloys, can satisfy the requirements nicely, making them the attractive BP material candidates for PEMFCs.[5] Among these metals, Ti and its alloys have received widespread attention in recent years owing to their high specific strength and anticorrosion performance.[6] However, there remain two major challenges for the practical application of Ti and its alloys: i) their surfaces are naturally covered with a nonconductive passivation layer, which hampers the power density of PEMFCs due to the interface contact resistance (ICR) between BP and gas diffusion layer (GDL); ii) although the passive oxide layer benefits the anticorrosion performance of Ti and its alloys, corrosion will inevitably occur in the acidic operating environment of PEMFCs, leading to the degradation of PEMFCs' performance.[6,7]

F. Yu, K. Wang, L. Cui, H. Peng, Z. Liu
Center for Nanochemistry (CNC)
Beijing Science and Engineering Center for Nanocarbons
Beijing National Laboratory for Molecular Sciences
College of Chemistry and Molecular Engineering
Peking University
Beijing 100871, P. R. China
E-mail: hlpeng@pku.edu.cn; zfliu@pku.edu.cn

F. Yu, K. Wang, P. Gao, H. Peng, Z. Liu
Beijing Graphene Institute (BGI)
Beijing 100095, P. R. China

L. Cui
State Key Laboratory of NBC Protection for Civilian
Beijing 102205, P. R. China

The ORCID identification number(s) for the author(s) of this article can be found under https://doi.org/10.1002/adma.202110565.

S. Wang, M. Hou
Laboratory of Fuel Cells
Dalian Institute of Chemical Physics
Chinese Academy of Sciences
Dalian 116023, P. R. China

F. Xiong, R. Zou
Beijing Key Lab of Advanced Battery Materials
Department of Materials Science and Engineering
College of Engineering
Peking University
Beijing 100871, P. R. China

P. Gao
Electron Microscopy Laboratory
and International Center for Quantum Materials
School of Physics
Peking University
Beijing 100871, P. R. China

DOI: 10.1002/adma.202110565

To overcome these two challenges, conductive and protective coatings have been generally adopted. As for Ti and its alloys, the coatings can be divided into three main categories, including pure metal, metallic nitrides or carbides, and carbon-based materials. For instance, noble metallic coatings, such as Pt,[8] Ag,[9] and Au,[10,11] were reported to effectively reduce the ICR and improve the corrosion resistance of Ti-based BPs. However, their commercialization is impeded by the high cost of noble metals. As an alternative, coatings of transition metallic nitrides or carbides (TiN,[12–14] Ta_2N,[15] TiC,[16] ZrC,[17] etc.) were extensively investigated thanks to their high electrical conductivity and chemical stability. Besides, carbon-based coatings often have a lower cost and a better performance, therefore displaying a great prospect of commercial application.[18] For example, Toyota in 2014 launched its first commercial fuel cell electric vehicle, Mirai, which utilized amorphous carbon-coated Ti for the cathode flow field.

Particularly, the rise of graphene, a monolayer of hexagonal carbon atoms, provides a new opportunity for enhancing the interfacial electrical conduction and corrosion resistance of metallic BPs.[19–21] On the one hand, the highest mobility of charge carriers and recorded thermal conductivity make graphene film an attractive interface material, so as to enhance electrical and thermal conductivities in PEMFCs.[22–24] On the other hand, graphene film has been successfully demonstrated to protect various metals from corrosion and oxidation due to its impermeability to molecules.[25–29] Along with its chemical stability and excellent mechanical strength, graphene film shows significant potentials as a conductive and protective coating for Ti-based BPs. Compared with common horizontal graphene, vertical graphene (VG) is characterized by a unique 3D structure, resulting in its excellent electrical and thermal conductivities in both the horizontal and vertical directions.[30–32] Moreover, the improved surface roughness endows VG with high hydrophobicity,[33] so as to provide an effective barrier to preventing the penetration of corrosive liquid. However, to the best of our knowledge, the investigation of VG film functioning as the conductive and protective coatings for metallic BPs in PEMFC operating environment has not been disclosed.

Herein, we report the direct growth of VG film on Ti alloy (TC4) by the plasma-enhanced chemical vapor deposition (PECVD) route. With the multifunctional VG coating, three benefits are reaped (**Figure 1**): i) as-grown VG exhibits strong interaction with Ti alloy substrate through a compact transition layer of Ti carbides; ii) the vertically oriented structure of VG enables superior electrical and thermal conduction between BP and GDL; iii) the highly hydrophobic VG coating effectively suppresses the penetration of corrosive liquid onto the substrate, as well as contributing to the water management in PEMFCs. As a consequence, VG–Ti alloy BP shows significantly enhanced interfacial electrical and thermal conductivities, corrosion resistance, and hydrophobicity compared with bare Ti alloy BP, which will be beneficial to the performance and stability of PEMFCs. Our findings contribute to the surface reinforcement of metals by the robust and versatile VG coating for the critical industrial applications.

2. Results and Discussion

PECVD has emerged as an important method of synthesizing graphene at a relatively low temperature.[34–36] A radio frequency (RF)-PECVD system was used in this work, which coupled energy from the RF fields to the plasma via an inductive coil (Figure S1, Supporting Information). The plasma was ignited by using CH_4 as the carbon source at an RF power of 300 W. After the growth with 20 sccm CH_4 for 2 h at 600 °C, the surface of VG–Ti alloy turned tawny in contrast to the silver-gray surface of bare Ti alloy (**Figure 2**a). Interestingly, as-grown graphene is characterized by vertically oriented morphology, named VG. As revealed by scanning electron microscopy (SEM) and atomic force microscopy (AFM) images in Figure 2b,c, the vertical

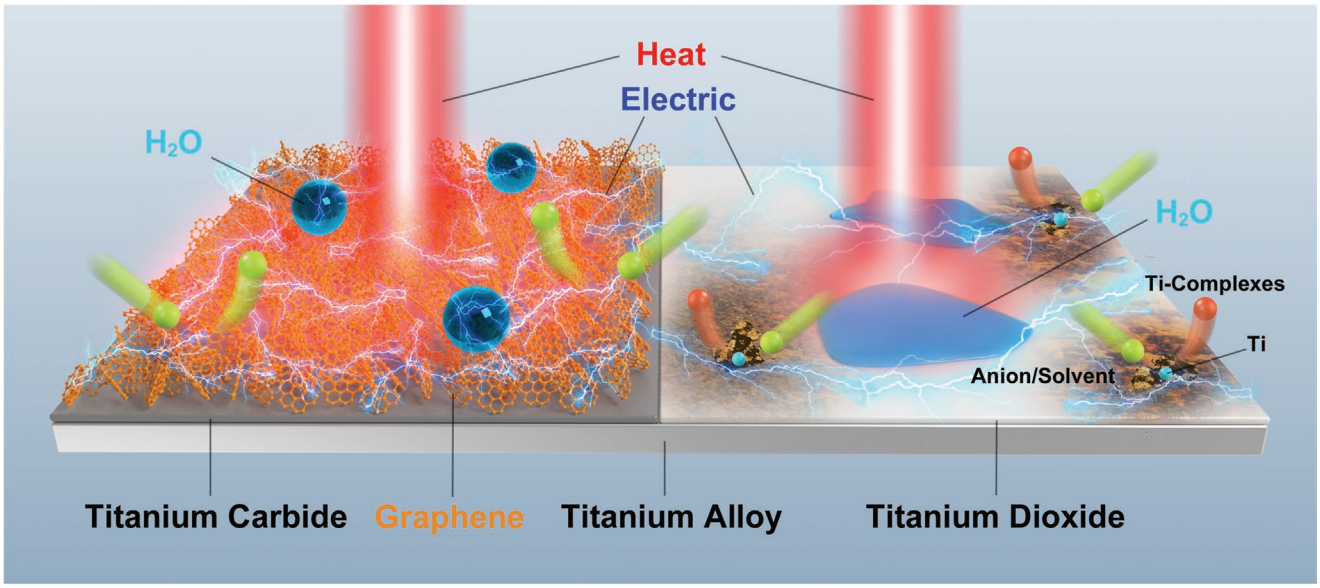

Figure 1. Schematic of VG–Ti alloy with enhanced electrical and thermal conductivities, corrosion resistance, and hydrophobicity.

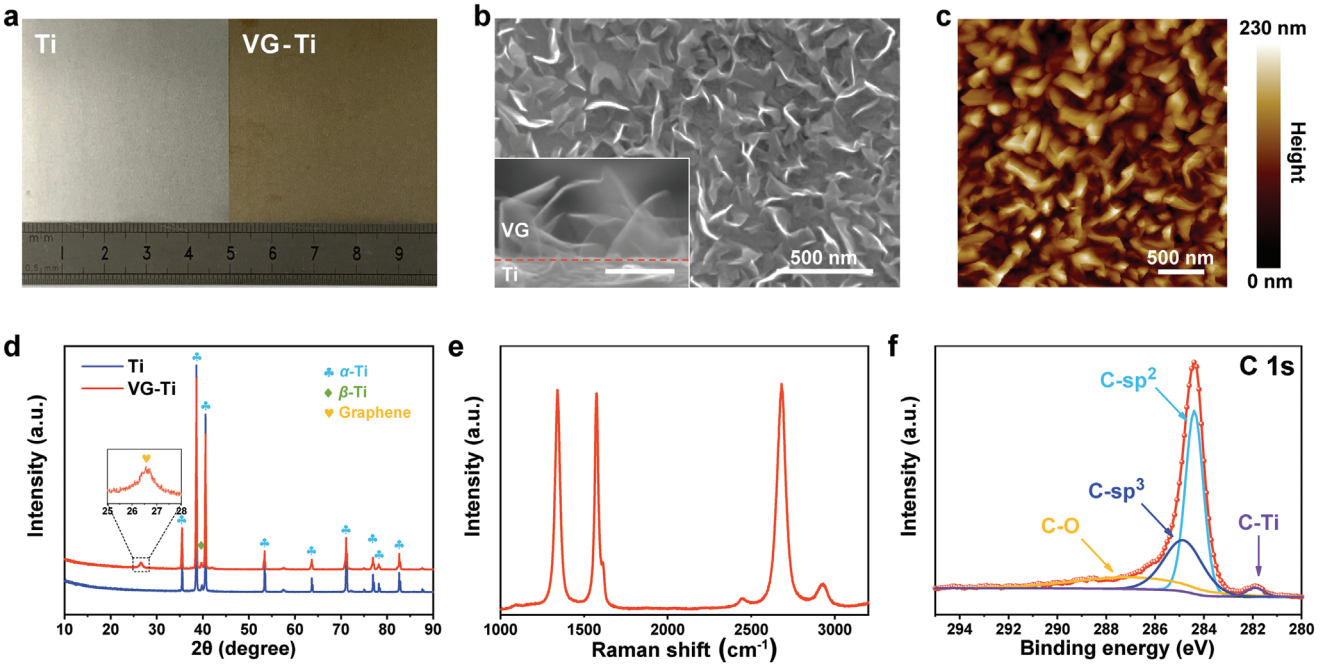

Figure 2. Direct growth of VG on Ti alloy by PECVD route. a) Photograph of bare Ti alloy and VG–Ti alloy. Growth conditions: 20 sccm CH_4 for 2 h at 600 °C. b) SEM image of VG. Inset: side-view SEM image of VG; scale bar: 200 nm. c) AFM image of VG. d) XRD patterns of bare Ti alloy and VG–Ti alloy. e) Typical Raman spectrum of VG. f) XPS signal of C 1s of VG. Ti refers to Ti alloy and VG–Ti refers to VG–Ti alloy in all figures of this paper.

heights and lateral sizes of VG are ≈100–230 and 200–300 nm, respectively. For the VG layer, an average thickness of ≈200 nm is observed from the inset of Figure 2b. As for the growth processes of VG, various active carbon species (CH_x, C_2H_y, atomic C and H, etc.) dissociated by CH_4 precursor were absorbed quickly onto the Ti alloy surface at the initial stage, leading to the formation of a horizontal carbon film (Figure S2a, Supporting Information).[37,38] Subsequently, the carbon film began curling upward caused by the factors of temperature gradient, intense ion bombardment, and lattice mismatch, giving rise to graphene nanowalls (Figure S2b, Supporting Information).[39,40] With the increasing growth time, graphene nanowalls extended into VG that fully covered the Ti alloy surface.

X-ray diffraction (XRD), Raman spectroscopy, and X-ray photoelectron spectroscopy (XPS) characterizations were carried out on VG, as presented in Figure 2d–f. After the plasma-enhanced process, the typical peak of pristine graphite can be identified at $2\theta = 26.6°$ (d spacing = 0.335 nm) in the XRD pattern (Figure 2d), corresponding to the stacking of graphene layers. Likewise, the Raman spectrum in Figure 2e displays the characteristic peaks of graphene at 1341 cm^{-1} (D band), 1575 cm^{-1} (G band), and 2681 cm^{-1} (2D band). The chemical composition of VG characterized by XPS measurement shows a strong sp^2 carbon peak (≈284.4 eV) (Figure 2f), indicating its high crystallinity at a relatively low growth temperature. Noticeably, a peak of ≈281.9 eV appears for VG–Ti alloy, related to the formation of Ti—C bonds, which will be discussed later.[41]

The controlled growth of VG with desirable characteristics is significant for its applications in gas sensors, supercapacitors, lithium-ion batteries, electrochemical transducers, etc.[42–45] The influences of growth temperature and methane flow rate were investigated by SEM and Raman characterizations. With the temperature rising from 500 to 600 °C, the lateral sizes and vertical heights of VG increased obviously (Figure S3a,b, Supporting Information). It is believed that a higher growth temperature can promote the dissociation of CH_4, thus favoring VG growth rate.[46] However, further increase of temperature to 700 °C led to smaller and more interlaced graphene nanosheets (Figure S3c, Supporting Information), which could be attributed to the massive increase of nucleation sites. Raman spectra reveal that the best crystal quality can be obtained at 600 °C with the lowest I_D/I_G and the highest I_{2D}/I_G intensity ratios (Figure S3d, Supporting Information). In addition, denser nanosheets are observed with the increase of CH_4 flow rates from 5 to 20 sccm because more active carbon species are introduced into the PECVD system (Figure S4, Supporting Information).

To clarify the interfacial structure, cross-sectional transmission electron microscopy (TEM) characterization was conducted on Ti alloy before and after the VG growth. **Figure 3**a–c reveals the formation of VG after the plasma-enhanced process, which is composed of a horizontal carbon film and vertical graphene nanowalls. Noticeably, a bright passive oxide layer with the thickness of ≈3 nm (outlined by black dashed lines in Figure 3a) existed on bare Ti alloy but disappeared after the growth of VG (Figure 3b,c), stemming from the reducing atmosphere in the PECVD system. This finding suggested that the VG coating can isolate air from the Ti alloy surface and therefore prevent its natural oxidation, which will benefit the electrical and thermal conduction between Ti alloy BP and GDL in PEMFCs.

More importantly, a compact and continuous transition layer with a thickness of ≈8 nm appeared between the VG coating and Ti alloy substrate of VG–Ti alloy sample (outlined by white dashed lines in Figure 3b,c). The chemical composition of the

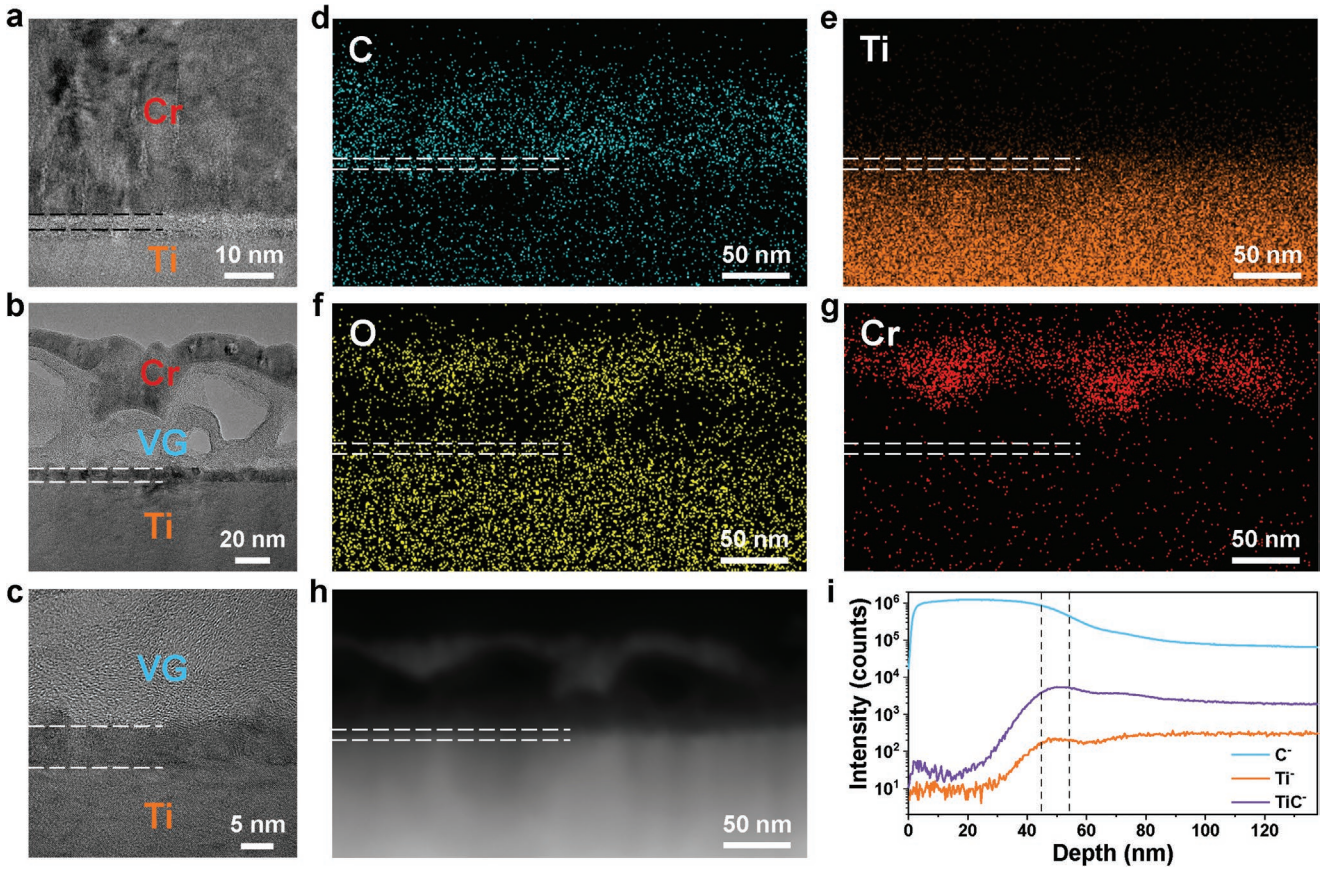

Figure 3. Characterization of the interface between the VG coating and Ti alloy substrate. a) Cross-sectional TEM image of bare Ti alloy. The black dashed line highlights the location of the passive oxide layer. b,c) Cross-sectional TEM images of VG–Ti alloy. Chromium (Cr) layers in panels (a) and (b) were thermally deposited to protect samples from possible damage during sample preparation. d–g) EDS elemental mappings of d) C, e) Ti, f) O, g) Cr, and h) corresponding HAADF image of VG–Ti alloy. The white dashed lines in panels (b–h) show the locations of the transition layer. i) ToF-SIMS analysis of VG–Ti alloy.

transition layer was investigated by energy-dispersive X-ray spectroscopy (EDS) elemental mappings (Figure 3d–g) corresponding to the high-angle annular dark-field (HAADF) image (Figure 3h). There displays an overlap between the Ti and C mappings (outlined by white dashed lines in Figure 3d,e), illustrating that the transition layer contains the elements of Ti and C. Time-of-flight secondary ion mass spectrometry (ToF-SIMS) was further employed to verify the surface chemical composition. The depth profiles of C^-, Ti^-, and TiC^- ions are presented in Figure 3i. It can be seen that the intensity of C^- ion decreases along the depth and finally stabilizes, while the intensity of Ti^- ion increases to a constant level. Interestingly, the decrease of C^- intensity and increase of Ti^- intensity both go through a gradually transforming stage instead of sharp variation within the depth of about 45–54 nm, where the intensity of TiC^- ion reaches the maximum value. Similarly, XPS depth profile analysis of VG–Ti alloy shows the C concentration slowly decreases and Ti concentration gradually increases with the sputtering time of ≈500–2000 s (Figure S5, Supporting Information), suggesting that there is no sharp interface between the VG layer and Ti alloy. Hence, the formation of the TiC transition layer can be confirmed, which is expected to provide the VG coating with stronger adhesion with the Ti alloy substrate.[47]

The ICR between the BP and GDL will greatly influence the power density of PEMFC due to undesired Ohmic loss.[48] We anticipate that the introduction of the VG coating onto Ti alloy will enhance the electrical conductivity between the BP and GDL (**Figure 4**a). As displayed in Figure 4b, the ICR measurement was performed on bare Ti alloy and VG–Ti alloy at the compaction pressure of 10–170 N cm^{-2}. For both the samples, the ICR values decrease strikingly at low compaction pressures but slowly at high pressures, which reveals that the surface composition replacing effective contact area becomes the decisive factor to interfacial conduction with the increase of pressure. Obviously, the ICRs of VG–Ti alloy (<10 mΩ cm^2) are rather lower than those of Ti alloy within the entire pressure range, meeting the DOE 2025 technical target (Table S1, Supporting Information).[49] Significantly, the ICR of VG–Ti alloy reaches 1.48 mΩ cm^2 at the pressure of 140 N cm^{-2} (typical compaction pressure for commercial PEMFCs), just ≈1% that of bare Ti alloy (150 mΩ cm^2). The lower ICR of VG–Ti alloy results from the excellent out-of-plane electrical conductivity of VG endowed by its vertically oriented structure, as well as the absence of the passivation layer on Ti alloy surface.

Efficient thermal management is indispensable for allowing rapid heat dissipation in PEMFC and, therefore, avoiding its

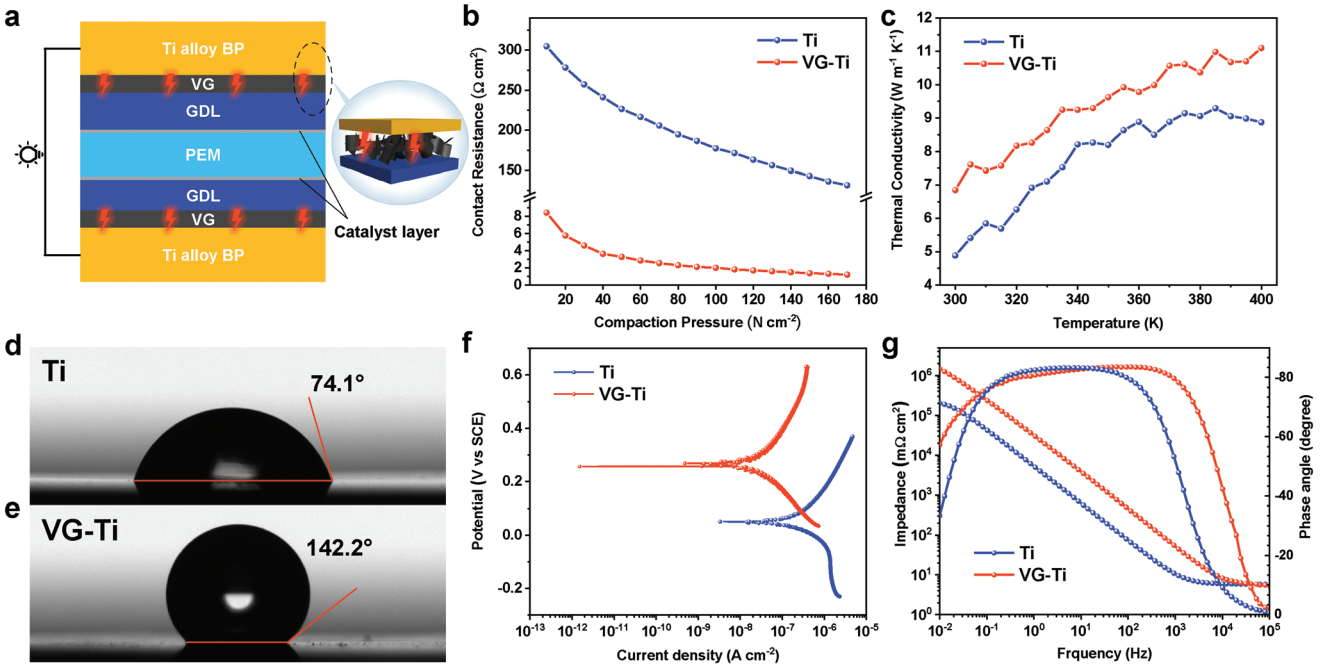

Figure 4. a) Schematic of the enhancement of interfacial electrical conduction for Ti–VG alloy. b) ICR as a function of compaction pressure for bare Ti alloy and VG–Ti alloy. c) Thermal conductivity as a function of temperature for bare Ti alloy and VG–Ti alloy. d,e) Water CAs of d) Ti alloy and e) VG–Ti alloy. f) Potentiodynamic polarization curves and g) Bode plots of bare Ti alloy and VG–Ti alloy in 0.5 M H_2SO_4 and 5 ppm HF solution at room temperature.

local overheating. As measured by the laser flash method,[50] the thermal conductivities of VG–Ti alloy are always higher than those of bare Ti alloy within the measuring temperature range of 300–400 K (Figure 4c). At the typical temperature of 350 K in PEMFCs, the thermal conductivity of VG–Ti alloy increases from 8.19 to 9.62 W m^{-1} K^{-1}, an improvement of ≈20% compared with that of bare Ti alloy. The results show the enhanced thermal transport property of VG–Ti alloy, brought by the high thermal conduction of the VG coating.

Besides thermal management, good water management is also required for PEMFCs to transport the reaction product water.[51] Therefore, the hydrophobicity of BP materials plays important roles in preventing the accumulation of water and distributing gaseous along flooding channels. The wettability of bare Ti alloy and VG–Ti alloy was assessed by using contact angle (CA) measurements. As displayed in Figure 4d,e, the water CA of VG–Ti alloy is ≈142.2°, which is greatly larger than that of Ti alloy (≈74.1°). The excellent hydrophobicity of VG–Ti alloy benefits from the vertically oriented rough surface of VG, which will contribute to the water management in the PEMFC system.

The hydrophobic VG coating is also expected to enhance the corrosion resistance of the underlying Ti alloy substrate, because the penetration of corrosive liquid can be restrained by the air layer existing between the VG surface and solution. The potentiodynamic polarization technique was employed on bare Ti alloy and VG–Ti alloy to qualitatively evaluate their corrosion resistance. The electrochemical reaction under kinetic control follows the Butler–Volmer formula, according to which the corrosion current density (J_{corr}) can be obtained by extrapolating the linear portion of the anodic and cathodic Tafel curves to the corrosion potential (E_{corr}). A lower J_{corr} and a more positive E_{corr} suggest better corrosion resistance of samples. Figure 4f shows the Tafel curves collected from bare Ti alloy and VG–Ti alloy in 0.5 M H_2SO_4 and 5 ppm HF solution at room temperature. Compared with Ti alloy, the Tafel curve of VG–Ti alloy presents a lower J_{corr} (≈0.0434 vs 0.523 μA cm^{-2}) and a higher E_{corr} (≈261 vs 50.3 mV). Furthermore, the corrosion rate (CR, μm yr^{-1}) can be calculated with the J_{corr} value[52]

$$CR = \frac{J_{corr} \times K \times EW}{\rho} \quad (1)$$

where the corrosion rate constant K = 3272 mm A^{-1} cm^{-1} yr^{-1}, the equivalent weight EW = 11.768 g for TC4 alloy, and the material density ρ = 4.45 g cm^{-3} for TC4 alloy. The calculated corrosion rate of VG–Ti alloy reduces by ≈12 times compared with that of bare Ti alloy (≈4.52 vs 0.376 μm yr^{-1}), indicating the greatly enhanced corrosion resistance of Ti alloy coated by VG. Electrochemical impedance spectroscopy (EIS) measurement was further carried out to determine the impedance, as presented by Bode plots in Figure 4g. In general, the coating with the impedance higher at the lowest frequency and the minimum phase angles closer to −90° is considered to offer better anticorrosion performance.[53] From Bode impedance plots, the impedance at the lowest frequency of VG–Ti alloy (≈1050 kΩ cm^2) is about five times greater than that of bare Ti alloy (≈200 kΩ cm^2). Meanwhile, Bode phase plots exhibit a slightly negative shift of the minimum phase angle after the introduction of the VG coating. And no obvious changes occurred on the surface of VG–Ti alloy in contrast to bare Ti alloy after EIS tests (Figure S6, Supporting Information). In

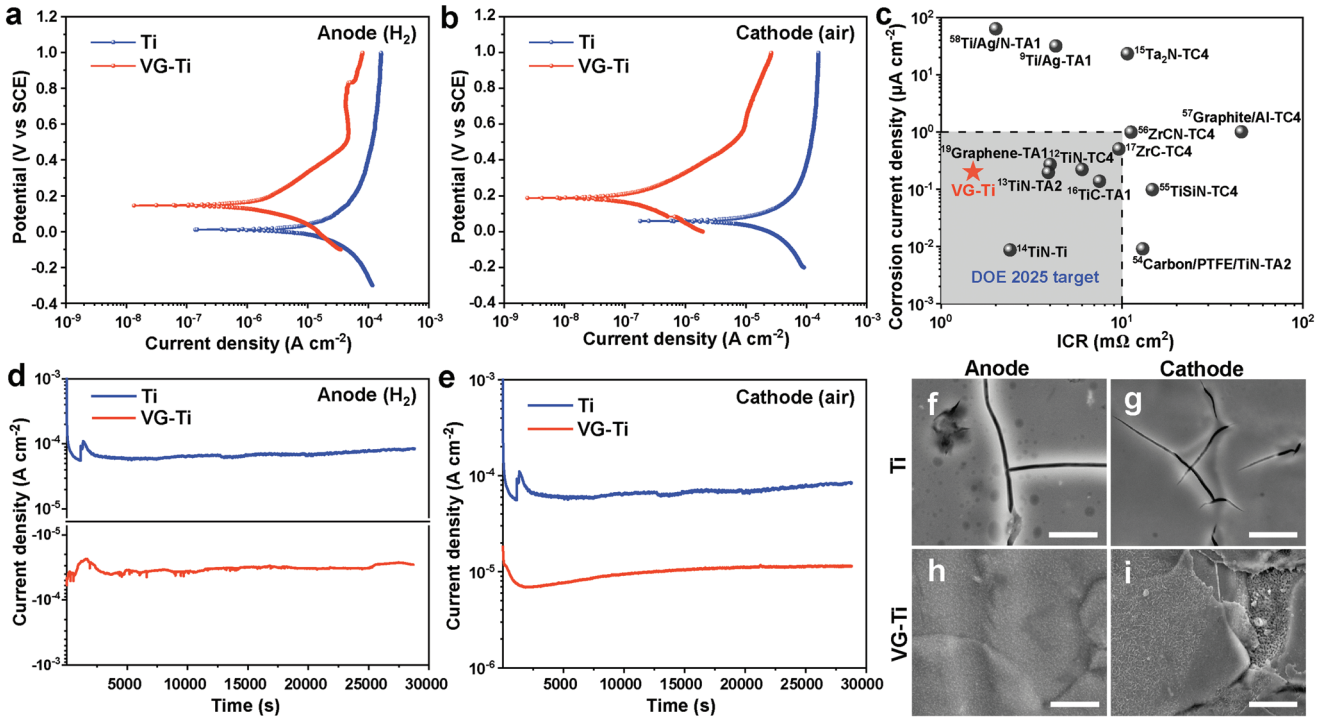

Figure 5. Anticorrosion performance of VG–Ti alloy under the simulated PEMFC operating environment. a,b) Potentiodynamic polarization curves for bare Ti alloy and VG–Ti alloy in 0.5 M H_2SO_4 and 5 ppm HF solution at 80 °C bubbled with H_2 or air to simulate the a) anodic or b) cathodic environment, respectively. c) Comparison of corrosion current density (*y*-axis) and ICR (*x*-axis) of various reported Ti-based BP materials. d,e) Potentiostatic polarization curves for Ti alloy and VG–Ti alloy in the simulated d) anodic and e) cathodic environments. f–i) SEM images of bare Ti alloy and VG–Ti alloy after the potentiostatic polarization measurement corresponding to the samples in panels (d) and (e). Scale bars: 2 μm.

brief, the electrochemical tests reveal VG as an effective and robust corrosion barrier for Ti alloy. This can be mainly interpreted that the hydrophobicity of VG together with its intrinsic impermeability suppresses the diffusion of corrosive liquid onto the Ti alloy surface. Additionally, the compact and continuous TiC transition layer forming between the VG coating and Ti alloy substrate may function as an extra diffusion barrier, as similarly reported for improving the corrosion resistance of Ti alloy (TA1) by the TiC-modified layer.[16]

To investigate the actual performance of VG–Ti alloy as a BP material, potentiodynamic and potentiostatic polarization were performed under the simulated PEMFC operating environment (0.5 M H_2SO_4 solution and 5 ppm HF solution at 80 °C bubbled with H_2 or air to simulate anodic or cathodic environment, respectively). As presented in potentiodynamic polarization curves (**Figure 5**a,b), VG–Ti alloy presents markedly lower corrosion current densities than those of bare Ti alloy (≈3.06 vs 32.9 μA cm^{-2} in the simulated anodic environment and ≈0.200 vs 26.2 μA cm^{-2} in the simulated cathodic environment). Moreover, the E_{corr} values of VG–Ti alloy show a positive shift compared with those of bare Ti alloy in both anodic and cathodic environments, suggesting a better thermodynamic stability of VG–Ti alloy. Significantly, the calculated corrosion rate of VG–Ti alloy is ≈1.73 μm yr^{-1} in the simulated cathodic environment, which is approximately two orders of magnitude less than that of bare Ti alloy (≈227 μm yr^{-1}). It is evident that the VG coating can enhance the corrosion resistance of Ti alloy under the PEMFC operating environment, confirming the impressive potential of VG–Ti alloy to serve as an anticorrosive BP material in PEMFCs. The corrosion current density and ICR of VG–Ti alloy and previous Ti-based BP materials are summarized in Figure 5c.[9,12–17,19,54–58] Compared with previously reported values, VG–Ti alloy exhibits the best interfacial electrical conductivity and satisfactory corrosion resistance.

Figure 5d indicates the potentiostatic polarization curves of bare Ti alloy and VG–Ti alloy at the anode potential of –0.1 V_{SCE}, from which the current density stabilizes at ≈90 μA cm^{-2} for bare Ti alloy and ≈–30 μA cm^{-2} for VG–Ti alloy. The negative current density of VG–Ti alloy suggests that the VG coating can effectively protect Ti alloy from being corroded in the simulated anodic environment. Likewise, the current density of VG–Ti alloy is about one-seventh that of bare Ti alloy (≈10 vs 70 μA cm^{-2}) in the simulated cathodic environment with a potential of 0.6 V_{SCE}, revealing a lower corrosion rate for VG–Ti alloy during the potentiostatic test (Figure 5e). Therefore, the VG coating exhibits long-term protection for Ti alloy, which will contribute to the stability of PEMFCs. The surface morphologies of Ti alloy and VG–Ti alloy after the potentiostatic polarization measurement are presented in SEM images (Figure 5f–i). As for bare Ti alloy samples, apparent cracks occurred after the exposure to an acidic testing environment at 80 °C for 8 h. In contrast, negligible corrosion trace could be observed on the surface of Ti alloy coated by VG, confirming the long-term corrosion protection of the VG coating. Notably, the VG coating remained intact after the polarization test in the simulated anodic environment (Figure 5h), therefore

still keeping a fairly low ICR for VG–Ti alloy (2.42 mΩ cm^2 at the pressure of 140 N cm^{-2}) (Figure S7, Supporting Information). Although the VG coating partially broke in the simulated cathodic environment (Figure 5i), the slightly increased ICR of 9.74 mΩ cm^2 can meet the DOE 2025 technical target (Figure S7, Supporting Information). These results suggest that the robust VG coating can play a durable role in enhancing corrosion resistance and electrical conductivity for Ti alloy BP materials in PEMFCs.

3. Conclusion

In summary, we demonstrated a robust and facile approach for the surface reinforcement of Ti alloy BP with the directly grown VG coating. The vertically oriented structure of VG enabled the excellent electrical and thermal conductivities between Ti alloy BP and GDL. Moreover, the VG coating exhibited high hydrophobicity and strong interaction with Ti alloy substrate, therefore, enhancing the corrosion resistance of Ti alloy in the simulated PEMFC environment. The VG–Ti alloy BP as designed can serve as a conductive and protective coating to improve the performance and stability of PEMFCs. This study provides an orientation-engineered strategy for graphene growth to reinforce metal surfaces, which may help to expand the applications of metals in high-performance electrodes, electronic devices, and industrial parts.

4. Experimental Section

PECVD Growth of VG: Commercially available Ti alloy (TC4) foil with a thickness of ≈100 µm was first ultrasonically cleaned in acetone and ethanol, successively. After being dried in blowing nitrogen gas, Ti alloy foil was placed at the hot center of the furnace. In a typical procedure, the RF-PECVD system (13.56 MHz) was evacuated to the base pressure (<1 Pa) using a mechanical vacuum pump and then heated to 500–700 °C under a H_2 flow of 20 sccm. Subsequently, 5–20 sccm CH_4 replacing H_2 was introduced into the system, and the plasma generator was turned on with a power of 300 W to generate CH_4 plasma. The growth of VG lasted for 0.5–2 h, followed by the natural cooling process to room temperature with 100 sccm Ar.

ICR Measurements: The ICRs of bare Ti alloy and VG–Ti alloy were measured before and after corrosion in the simulated PEMFC operating environment. The samples were sandwiched between two GDLs and then placed between two Cu electrodes plated with Au. The details of ICR measurements could be found in the literatures.[59,60]

Electrochemical Tests: Electrochemical tests were carried out using a three-electrode method on a CHI760C electrochemical workstation. The three-electrode system included the investigated sample with an exposure area of 0.785 cm^2 as the working electrode, platinum tablet as the counter electrode, and saturated calomel electrode (SCE) as the reference electrode. Potentiodynamic polarization and EIS tests were first performed in 0.5 M H_2SO_4 and 5 ppm HF solution at room temperature. Open-circuit potential (OCP) was monitored for 1 h to confirm its stability. Potentiodynamic polarization was conducted at a scan rate of 1.0 mV s^{-1}. EIS data were recorded at the frequency range from 10^5 to 0.01 Hz by using a sinusoidal perturbation of 10 mV amplitude around the OCP. Potentiodynamic and potentiostatic polarization were further measured in 0.5 M H_2SO_4 solution and 5 ppm HF solution at 80 °C bubbled with H_2 or air to simulate the anodic or cathodic environment, respectively. Potentiostatic polarization for 8 h was applied at the anodic (−0.1 V_{SCE}) and cathodic (0.6 V_{SCE}) operating potentials.

Characterization: The prepared samples were characterized using SEM (Thermo Scientific Quattro S, acceleration voltage 10 kV), AFM (Bruker Dimension Icon with ScanAsyst mode), XRD (Bruker D8 ADVANCE), Raman spectroscopy (Horiba, LabRAM HR800, 532 nm laser wavelength), XPS (Kratos Analytical Axis-Ultra spectrometer with Al Kα X-ray source), ToF-SIMS (ION-ToF ToF.SIMS 5–100), CA system (DataPhysics OCA20), and TEM (FEI Titan, acceleration voltage 200 kV). The cross-sectional TEM samples were fabricated using a focused ion beam system (FET Strata DB 235). The thermal conductivity was determined using a laser flash analyzer (NETZSCH LFA 467 HyperFlash).

Supporting Information

Supporting Information is available from the Wiley Online Library or from the author.

Acknowledgements

F.Y., K.W., and L.Z.C. contributed equally to this work. This work was financially supported by Beijing National Laboratory for Molecular Sciences (BNLMS-CXTD-202001), the National Natural Science Foundation of China (Grant Nos. 51432002, U1904193, T2188101, and 52021006), and Beijing Municipal Science & Technology Commission Project (Project No. Z201100008720001). F.Y. acknowledges the support from International Postdoctoral Exchange Fellowship Program 2018 (Talent-Introduction Program).

Conflict of Interest

The authors declare no conflict of interest.

Data Availability Statement

The data that support the findings of this study are available from the corresponding author upon reasonable request.

Keywords

corrosion resistance, hydrophobicity, interfacial contact resistance, plasma-enhanced chemical vapor deposition, titanium alloy bipolar plates, vertical graphene

Received: December 27, 2021
Revised: March 18, 2022
Published online: April 25, 2022

[1] M. E. Scofield, H. Liu, S. S. Wong, *Chem. Soc. Rev.* **2015**, *44*, 5836.
[2] N. de las Heras, E. P. L. Roberts, R. Langton, D. R. Hodgson, *Energy Environ. Sci.* **2009**, *2*, 206.
[3] B. R. Padhy, R. G. Reddy, *J. Power Sources* **2006**, *153*, 125.
[4] H. Chen, H. B. Liu, L. Yang, J. X. Li, L. Yang, *Int. J. Hydrogen Energy* **2010**, *35*, 3105.
[5] S. Karimi, N. Fraser, B. Roberts, F. R. Foulkes, *Adv. Mater. Sci. Eng.* **2012**, *2012*, 828070.
[6] N. F. Asri, T. Husaini, A. B. Sulong, E. H. Majlan, W. R. W. Daud, *Int. J. Hydrogen Energy* **2017**, *42*, 9135.
[7] D. P. Davies, P. L. Adcock, M. Turpin, S. J. Rowen, *J. Appl. Electrochem.* **2000**, *30*, 101.

[8] H. Y. Jung, S. Y. Huang, B. N. Popov, *J. Power Sources* **2010**, *195*, 1950.
[9] H. Zhang, M. Hou, G. Lin, Z. Han, Y. Fu, S. Sun, Z. Shao, B. Yi, *Int. J. Hydrogen Energy* **2011**, *36*, 5695.
[10] H. Y. Jung, S. Y. Huang, P. Ganesan, B. N. Popov, *J. Power Sources* **2009**, *194*, 972.
[11] S. H. Wang, J. Peng, W. B. Lui, J. S. Zhang, *J. Power Sources* **2006**, *162*, 486.
[12] J. Jin, Z. He, X. Zhao, *Int. J. Hydrogen Energy* **2020**, *45*, 12489.
[13] P. Yi, C. Dong, T. Zhang, K. Xiao, Y. Ji, J. Wu, X. Li, *J. Power Sources* **2019**, *418*, 42.
[14] D. Zhang, L. Duan, L. Guo, Z. Wang, J. Zhao, W. H. Tuan, K. Niihara, *Int. J. Hydrogen Energy* **2011**, *36*, 9155.
[15] J. J. Ma, J. Xu, S. Jiang, P. Munroe, Z. H. Xie, *Ceram. Int.* **2016**, *42*, 16833.
[16] J. Shi, P. Zhang, Y. Han, H. Wang, X. Wang, Y. Yu, J. Sun, *Int. J. Hydrogen Energy* **2020**, *45*, 10050.
[17] J. Xu, Z. Li, S. Xu, P. Munroe, Z. H. Xie, *J. Power Sources* **2015**, *297*, 359.
[18] Y. Show, *Surf. Coat. Technol.* **2007**, *202*, 1252.
[19] J. Wang, L. Min, F. Fang, W. Zhang, Y. Wang, *Int. J. Hydrogen Energy* **2019**, *44*, 16909.
[20] N. W. Pu, G. N. Shi, Y. M. Liu, X. Sun, J. K. Chang, C. L. Sun, M. D. Ger, C. Y. Chen, P. C. Wang, Y. Y. Peng, C. H. Wu, S. Lawes, *J. Power Sources* **2015**, *282*, 248.
[21] A. C. Stoot, L. Camilli, S. A. Spiegelhauer, F. Yu, P. Bøggild, *J. Power Sources* **2015**, *293*, 846.
[22] X. Du, I. Skachko, A. Barker, E. Y. Andrei, *Nat. Nanotechnol.* **2008**, *3*, 491.
[23] A. A. Balandin, S. Ghosh, W. Bao, I. Calizo, D. Teweldebrhan, F. Miao, C. N. Lau, *Nano Lett.* **2008**, *8*, 902.
[24] C. Chang, W. Chen, Y. Chen, Y. Chen, Y. Chen, F. Ding, C. Fan, H. J. Fan, Z. Fan, C. Gong, Y. Gong, Q. He, X. Hong, S. Hu, W. Hu, W. Huang, Y. Huang, W. Ji, D. Li, L. J. Li, Q. Li, L. Lin, C. Ling, M. Liu, N. Liu, Z. Liu, K. P. Loh, J. Ma, F. Miao, H. Peng, et al., *Acta Phys.-Chim. Sin* **2021**, *37*, 2108017.
[25] M. Wang, M. Tang, S. Chen, H. Ci, K. Wang, L. Shi, L. Lin, H. Ren, J. Shan, P. Gao, Z. Liu, H. Peng, *Adv. Mater.* **2017**, *29*, 1703882.
[26] X. Xu, D. Yi, Z. Wang, J. Yu, Z. Zhang, R. Qiao, Z. Sun, Z. Hu, P. Gao, H. Peng, Z. Liu, D. Yu, E. Wang, Y. Jiang, F. Ding, K. Liu, *Adv. Mater.* **2018**, *30*, 1702944.
[27] F. Yu, L. Camilli, T. Wang, D. M. A. Mackenzie, M. Curioni, R. Akid, P. Bøggild, *Carbon* **2018**, *132*, 78.
[28] S. Chen, L. Brown, M. Levendorf, W. Cai, S. Y. Ju, J. Edgeworth, X. Li, C. W. Magnuson, A. Velamakanni, R. D. Piner, J. Kang, J. Park, R. S. Ruoff, *ACS Nano* **2011**, *5*, 1321.
[29] J. S. Bunch, S. S. Verbridge, J. S. Alden, A. M. van der Zande, J. M. Parpia, H. G. Craighead, P. L. McEuen, *Nano Lett.* **2008**, *8*, 2458.
[30] J. Shan, S. Wang, F. Zhou, L. Cui, Y. Zhang, Z. Liu, *Nano Lett.* **2020**, *20*, 5097.
[31] H. Ci, H. Chang, R. Wang, T. Wei, Y. Wang, Z. Chen, Y. Sun, Z. Dou, Z. Liu, J. Li, P. Gao, Z. Liu, *Adv. Mater.* **2019**, *31*, 1901624.
[32] S. Xu, S. Wang, Z. Chen, Y. Sun, Z. Gao, H. Zhang, J. Zhang, *Adv. Funct. Mater.* **2020**, *30*, 2003302.
[33] C. Yang, H. Bi, D. Wan, F. Huang, X. Xie, M. Jiang, *J. Mater. Chem. A* **2013**, *1*, 770.
[34] L. Cui, Y. Huan, J. Shan, B. Liu, J. Liu, H. Xie, F. Zhou, P. Gao, Y. Zhang, Z. Liu, *ACS Nano* **2020**, *14*, 15327.
[35] K. Wang, S. Cheng, Q. Hu, F. Yu, Y. Cheng, K. Huang, H. Yuan, J. Jiang, W. Li, J. Li, S. Xu, J. Yin, Y. Qi, Z. Liu, *Nano Res.* **2021**, https://doi.org/10.1007/s12274-021-3953-3.
[36] Y. Cheng, K. Wang, Y. Qi, Z. Liu, *Acta Phys.-Chim. Sin.* **2020**, *37*, 2006046.
[37] I. B. Denysenko, S. Xu, J. D. Long, P. P. Rutkevych, N. A. Azarenkov, K. Ostrikov, *J. Appl. Phys.* **2004**, *95*, 2713.
[38] A. Malesevic, R. Vitchev, K. Schouteden, A. Volodin, L. Zhang, G. V. Tendeloo, A. Vanhulsel, C. V. Haesendonck, *Nanotechnology* **2008**, *19*, 305604.
[39] J. Zhao, M. Shaygan, J. Eckert, M. Meyyappan, M. H. Rummeli, *Nano Lett.* **2014**, *14*, 3064.
[40] M. Zhu, J. Wang, B. C. Holloway, R. A. Outlaw, X. Zhao, K. Hou, V. Shutthanandan, D. M. Manos, *Carbon* **2007**, *45*, 2229.
[41] Y. Choi, T. Umebayashi, M. Yoshikawa, *J. Mater. Sci.* **2004**, *39*, 1837.
[42] J. Li, Z. Liu, Q. Guo, S. Yang, A. Xu, Z. Wang, G. Wang, Y. Wang, D. Chen, G. Ding, *J. Mater. Chem. C* **2019**, *7*, 5995.
[43] Z. Bo, W. Zhu, W. Ma, Z. Wen, X. Shuai, J. Chen, J. Yan, Z. Wang, K. Cen, X. Feng, *Adv. Mater.* **2013**, *25*, 5799.
[44] M. Wang, H. Yang, K. Wang, S. Chen, H. Ci, L. Shi, J. Shan, S. Xu, Q. Wu, C. Wang, M. Tang, P. Gao, Z. Liu, H. Peng, *Nano Lett.* **2020**, *20*, 2175.
[45] O. Akhavan, E. Ghaderi, R. Rahighi, *ACS Nano* **2012**, *6*, 2904.
[46] J. Wang, M. Zhu, R. A. Outlaw, X. Zhao, D. M. Manos, B. C. Holloway, *Carbon* **2004**, *42*, 2867.
[47] F. Zhou, B. Liu, Z. Li, J. Zhou, J. Shan, L. Cui, J. Hu, W. Quan, K. Cui, P. Gao, Y. Zhang, *ACS Nano* **2021**, *15*, 10514.
[48] Y. C. Park, S. H. Lee, S. K. Kim, S. Lim, D. H. Jung, D. Y. Lee, S. Y. Choi, H. Ji, D. H. Peck, *Int. J. Hydrogen Energy* **2010**, *35*, 4320.
[49] Y. Song, C. Zhang, C. Y. Ling, M. Han, R. Y. Yong, D. Sun, J. Chen, *Int. J. Hydrogen Energy* **2020**, *45*, 29832.
[50] P. Goli, H. Ning, X. Li, C. Y. Lu, K. S. Novoselov, A. A. Balandin, *Nano Lett.* **2014**, *14*, 1497.
[51] M. Qi, Y. Zeng, M. Hou, Y. Gou, W. Song, H. Chen, G. Wu, Z. Jia, Y. Gao, H. Zhang, Z. Shao, *Appl. Catal. B* **2021**, *298*, 120504.
[52] J. Yang, H. Yang, H. Yu, Z. Wang, X. Zeng, *Metall. Mater. Trans. A* **2017**, *48*, 3583.
[53] J. H. Huh, S. H. Kim, J. H. Chu, S. Y. Kim, J. H. Kim, S. Y. Kwon, *Nanoscale* **2014**, *6*, 4379.
[54] P. Gao, Z. Xie, X. Wu, C. Ouyang, T. Lei, P. Yang, C. Liu, J. Wang, T. Ouyang, Q. Huang, *Int. J. Hydrogen Energy* **2018**, *43*, 20947.
[55] S. Peng, J. Xu, Z. Li, S. Jiang, P. Munroe, Z. H. Xie, H. Lu, *Ceram. Int.* **2020**, *46*, 2743.
[56] J. Xu, H. J. Huang, Z. Li, S. Xu, H. Tao, P. Munroe, Z. H. Xie, *J. Alloys Compd.* **2016**, *663*, 718.
[57] A. M. Oladoye, J. G. Carton, A. G. Olabi, *J. Mater.* **2014**, *2014*, 914817.
[58] M. Zhang, L. Hu, G. Lin, Z. Shao, *J. Power Sources* **2012**, *198*, 196.
[59] Y. Wang, D. O. Northwood, *J. Power Sources* **2009**, *191*, 483.
[60] H. Wang, *J. Power Sources* **2003**, *115*, 243.